Journal of Materials Chemistry C

ROYAL SOCIETY OF CHEMISTRY

PAPER

View Article Online
View Journal

Cite this: DOI: 10.1039/d5tc04439a

Trap-mediated photogating in hybrid organic–inorganic heterojunction phototransistors for photo-memory and photodetection

Ahasan Ullah,[a] Roshell Lamug,[b] Xueqiao Zhang,[a] Oksana Ostroverkhova[b] and Li-Jing Cheng *[a]

Trap-mediated photocarrier dynamics fundamentally govern the photoresponse of hybrid organic–inorganic heterojunction phototransistors. In phototransistors with type-II heterojunctions, photoinduced electron transfer from the organic layer to the channel leaves holes trapped in the organic layer, inducing photogating that modulates channel conductance. Depending on trapping kinetics, these devices can function as fast photodetectors or light-programmable synaptic memories. We develop a compact, physics-based current-to-charge conversion model that quantitatively links transient drain current to trapped-hole density. The model incorporates shallow and deep trap populations with distinct kinetics and introduces a closed-form recurrence relation to describe conductance evolution under pulsed illumination. Validated on TIPS-Tc/IGZO and TES-ADT/IGZO phototransistors, the model accurately reproduces single- and multi-pulse responses and yields physically meaningful trap parameters. Deep-trap dominance in TIPS-Tc enables long retention and near-linear synaptic plasticity, whereas TES-ADT, dominated by shallow traps, exhibits a rapid photodetection response. In the TIPS-Tc/IGZO device, gate-voltage polarity modulation further allows programmable switching between memory retention, natural relaxation, and active forgetting by controlling charge distribution and trapping kinetics in the organic layer, thereby tuning the photogating strength. The deep-to-shallow trap ratio is identified as a key figure of merit governing the trade-off between retention, linearity, sensitivity, and speed. Requiring only minimal transient measurements and providing kinetically interpretable parameters, the model offers a predictive tool for material screening, device optimization, and array-scale design of light-programmable optoelectronic memory and high-speed photodetector systems.

Received 19th December 2025,
Accepted 8th March 2026

DOI: 10.1039/d5tc04439a

rsc.li/materials-c

1. Introduction

Hybrid organic–inorganic phototransistors are typically built on an organic/oxide semiconductor heterojunction, where the organic layer functions as a light absorber and the oxide channel enables charge transport. This architecture merges the strong and tunable optical absorption of organics with the high carrier mobility and stability of oxides such as amorphous indium gallium zinc oxide (IGZO).[1–5] Organic semiconductors offer low-cost, flexible, and solution processible platforms for optoelectronic devices,[1–3] but their carriers are readily trapped by structural defects and impurities, limiting mobility and response speed.[6–8] In the heterojunction, illumination generates electron–hole pairs in the organic layer; electrons transfer to the oxide channel, while holes accumulate at the interface and electrostatically modulate the oxide channel through photogating.[9–11] Acene derivatives such as tetracene and anthradithiophene (ADT) are particularly effective absorbers because their strong visible absorption, long exciton diffusion length, and favorable energy-level alignment with IGZO enable efficient photoinduced charge transfer and high photogating gain.[12,13] These acene layers also introduce trap states that strongly govern the phototransistor's temporal dynamics.[2] The organic component thus dictates both the spectral response and the trap landscape of the device. A recent study on perovskite–organic heterojunctions shows that tuning from type II to type I band alignment can enhance responsivity and photogain, while controlling molecular orientation improves photocarrier cycling efficiency.[14] Nevertheless, many organic–inorganic heterojunction devices rely on deep-trap-assisted photogating, where traps prolong the gated state after illumination—advantageous for synaptic memory but detrimental to

[a] School of Electrical Engineering and Computer Science, Oregon State University, Corvallis, Oregon, 97331, USA. E-mail: chengli@oregonstate.edu
[b] Department of Physics, Oregon State University, Corvallis, Oregon, 97331, USA

high-speed detection.[15,16] Quantifying how trap depth, density, and kinetics govern the drain-current transient is therefore crucial for optimizing hybrid phototransistors across both memory and detector applications.

Trapping in organic semiconductors arises from structural defects, dipoles, impurities, and local energetic disorder.[17] The trapping kinetics are described by carrier capture and release rate constants: the capture rate depends on the free-carrier density, capture cross section, and number of available empty traps, whereas the release rate is thermally activated and exponentially dependent on trap depth.[18] Shallow traps lie near the relevant band edge—the highest occupied molecular orbital (HOMO) for hole transport or the lowest unoccupied molecular orbital (LUMO) for electron transport—and readily exchange carriers with the band. In contrast, deep traps are positioned farther from the band edge and are less accessible through thermal excitation. Previous research has primarily focused on shallow traps, as deep states are difficult to detect experimentally and rarely induce substantial changes in charge carrier mobility.[19,20]

Most prior studies have also examined pristine organic-channel devices, where the organic semiconductor simultaneously conducts current and hosts trap states, making it difficult to decouple transport from trapping and to quantify the trap density of states (tDOS). This study separates charge transport from trapping phenomena using an organic–inorganic heterojunction architecture, in which a metal-oxide semiconductor channel provides charge transport, while an organic photoactive layer functions as a trap-mediated, persistent photogating element. Analysis of the temporal evolution of the photogating response, specifically through the extraction of trapping and detrapping time constants, enables independent identification and quantification of shallow and deep trap populations. This approach provides a robust and interpretable framework for elucidating the interplay of trap states in organic semiconductors. Most current descriptions of trap-assisted photogating are qualitative.[21,22] Without a quantitative model, it is challenging to extract key parameters like trap densities, capture cross-sections, or activation energies from experiments. This makes it hard to predict trade-offs between responsivity, response speed, and memory retention. Synaptic devices need a slow decay to mimic long-term potentiation, while photodetectors work best with fast recovery and negligible hysteresis. In hybrid acene–indium gallium zinc oxide (IGZO) systems, the balance between shallow and deep traps shapes these behaviors, but a complete kinetic model is still missing.

In this work, we develop a physics-based theoretical framework for interpreting drain-current transients in acene/IGZO heterojunction phototransistors, focusing on trap-mediated dynamics. The model converts measured optically induced drain-current responses into total trapped-hole densities and distinguishes shallow and deep trap populations, each characterized by distinct capture and release rates. A closed-form recurrence relation links the trapped state across illumination and dark intervals, enabling accurate prediction of both short-term and long-term photoresponses. The framework is validated using two representative heterojunction phototransistors based on (1) a 5,12-bis(triisopropylsilylethynyl)tetracene (TIPS-Tc)/IGZO exhibiting persistent photo-memory dominated by deep traps, and (2) a 2,8-difluoro-5,11-bis(triethylsilylethynyl) anthradithiophene (TES-ADT)/IGZO showing rapid recovery governed by shallow traps (Fig. 1a). Extracted parameters correspond directly to the kinetics of trap states and reproduce experimental transients with high fidelity. The model further reveals how the deep-to-shallow trap ratio dictates linearity, dynamic range, response speed, and sensitivity, providing quantitative design guidelines for next-generation hybrid phototransistors.

2. Results and discussion

2.1 Device structure and photogating mechanism

The devices are planar organic–inorganic heterojunction phototransistors comprising a 50 nm thick organic semiconductor layer (TIPS-Tc or TES-ADT) coated on 25 nm thick IGZO thin-film transistor (TFT) channels fabricated on thermally oxidized heavily doped p-type silicon substrates (Fig. 1a). The silicon substrate served as the bottom gate, and a 300 nm SiO_2 layer acted as the gate dielectric. The top aluminum source and drain electrodes define the channel width and length of 1000 × 100 μm. The organic layers were solution-processed on IGZO to form the heterojunctions (see Experimental section for details). Fig. 1b presents the molecular structures of TIPS-Tc and TES-ADT.

Both organics belong to the acene family and show strong visible absorption from 450 to 650 nm with three characteristic vibronic bands. The main absorption peaks (wavelength) center at 537 nm for TIPS-Tc and 548 nm for TES-ADT, while IGZO is optically transparent in this range (Fig. 1c). The frontier orbital energies of the organics (HOMO ≈ −5.35 to −5.40 eV; LUMO ≈ −3.05 to −3.0 eV),[12,23] aligned with IGZO to form a type II heterojunction that promotes interfacial exciton dissociation (Fig. 1a). Upon illumination, photoexcited electrons transfer into the IGZO channel, leaving holes in the organic layer that become trapped at or near the heterojunction interface. The trapped holes electrostatically modulate the IGZO channel, resulting in a photogating current that can remain after the light is turned off if deep traps dominate.

Fig. 2a–c show the transfer characteristics of TIPS-Tc/IGZO, TES-ADT/IGZO, and bare IGZO phototransistors. Measurements taken in darkness, under optical excitation, and after illumination highlight the roles of interfacial charge transfer and trapped-charge-induced photogating. In the TIPS-Tc/IGZO device (Fig. 2a), 535 nm (10 μW cm^{-2}) illumination increases the off-current and shifts the threshold voltage negatively, indicating electron transfer to the IGZO channel and photogating, respectively. After the light is turned off, the off-current returns to its dark level, confirming the cessation of electron transfer, while the threshold shift remains, signifying the persistence of long-lived trapped charge. These observations were verified by a dark sweep collected 60 s after light-off. The TES-ADT/IGZO device exhibits a similar negative threshold

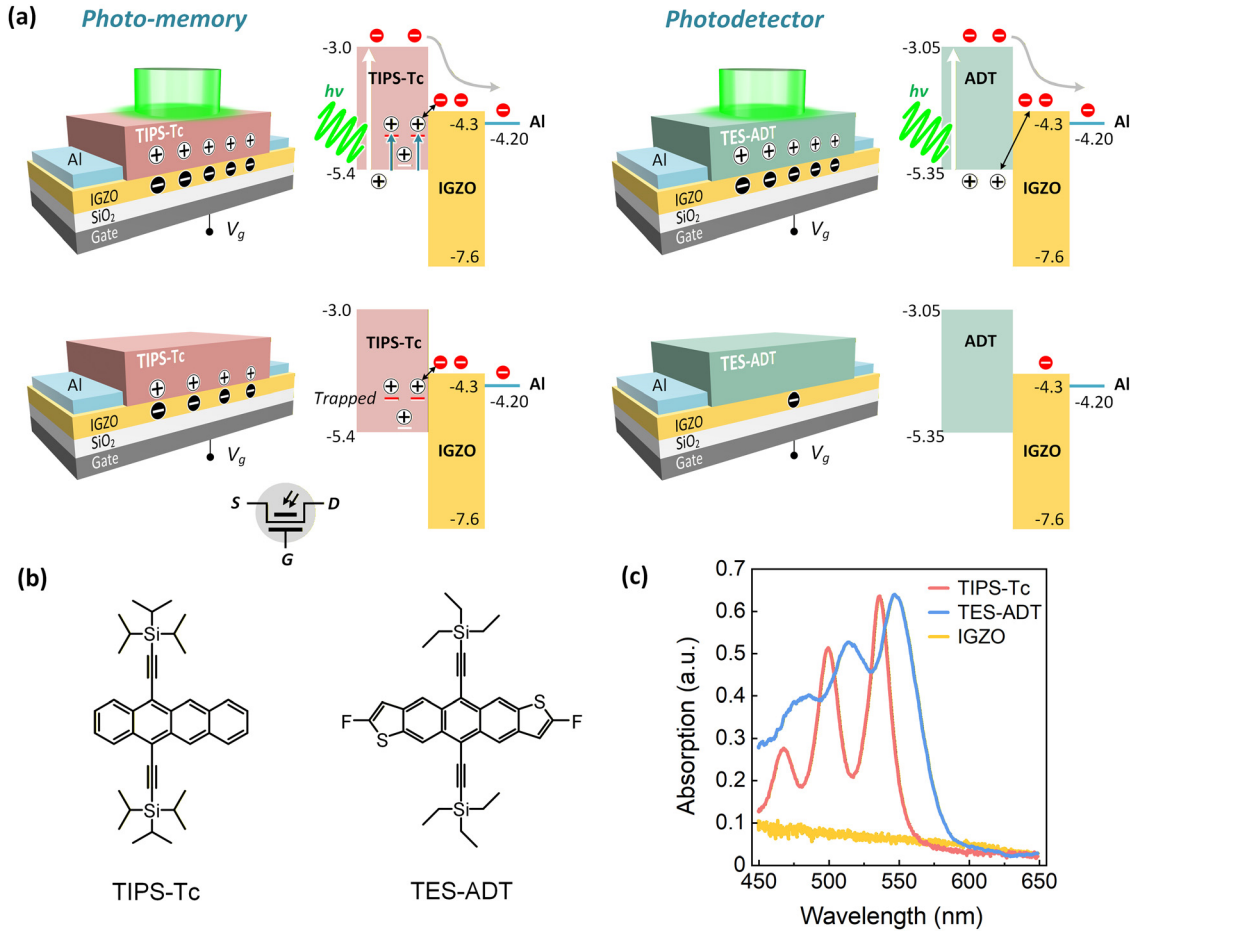

Fig. 1 (a) Schematics and energy band diagrams of the organic/IGZO heterojunction phototransistors, highlighting photo-memory operation through photogenerated charge trapping in the TIPS-Tc/IGZO heterojunction device and photodetector operation in the ADT/IGZO heterojunction device with minimal charge trapping. Inset: Symbol of the hybrid heterojunction phototransistor. (b) Molecular structures of TIPS-Tc and TES-ADT. (c) Optical absorption spectra of TIPS-Tc, TES-ADT, and IGZO, showing distinct absorption peaks at 537 nm (TIPS-Tc) and 548 nm (TES-ADT), with IGZO remaining largely transparent across 450–650 nm.

voltage shift and off-current increase under 545 nm excitation, consistent with interfacial charge transfer (Fig. 2b). However, the entire transfer characteristic returns to the dark level once illumination ceases. In contrast, the bare IGZO TFT shows no significant change (Fig. 2c), confirming that the observed effects originate from the organic–oxide heterojunction rather than IGZO oxygen-vacancy states, since 535 nm photons lack sufficient energy to activate those transitions.

The subthreshold swing (SS) extracted from the transfer characteristics under dark conditions is comparable for TES-ADT/IGZO (304.4 mV/dec) and TIPS-Tc/IGZO (337.4 mV/dec), confirming that SS is primarily governed by the IGZO/gate-oxide interface. Under illumination, however, the two devices respond differently: SS increases markedly in TES-ADT/IGZO (573.7 mV/dec) but changes only slightly in TIPS-Tc/IGZO (352.6 mV/dec). In both devices, illumination generates holes that become trapped near the organic/IGZO interface, and the applied gate field drives their redistribution during the transfer sweep. The different SS responses arise from distinct trapping and detrapping kinetics. In TES-ADT/IGZO, the relatively fast kinetics allow the trapped-hole population to dynamically follow the changing V_g. As V_g becomes more negative and suppresses channel conductance, the redistribution of trapped holes toward the TES-ADT/IGZO interface strengthens the photogating effect, partially counteracting the gate-induced depletion. This dynamic interplay between the gate field and photogating reduces effective gate control and broadens the subthreshold region, leading to a pronounced increase in SS. In contrast, the slower, deep-trap-dominated kinetics in TIPS-Tc/IGZO limit charge redistribution during the V_g sweep, so illumination mainly induces a threshold voltage shift with minimal impact on SS.

To further investigate interfacial charge transfer in the hybrid devices, steady-state and transient photoluminescence (PL) measurements were performed, as shown in Fig. 2d (see SI S1 for TES-ADT) and the Fig. 2d inset. The steady-state PL intensity of a TIPS-Tc/IGZO hybrid film is lower than that of a bare TIPS-Tc film. In addition, the average transient PL lifetime decreases from 4.5 ns to 1.5 ns, confirming efficient exciton dissociation and electron transfer to IGZO. The decay curves

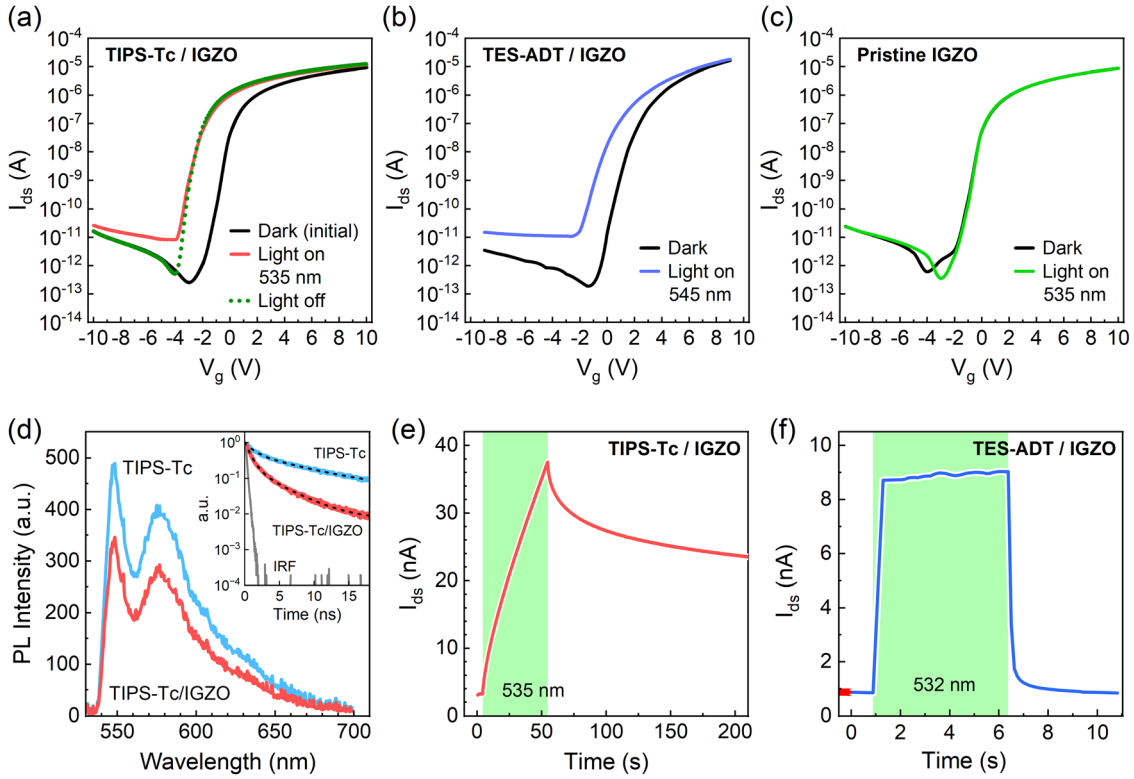

Fig. 2 Experimental evidence of charge transfer and photogating in hybrid organic/inorganic phototransistors. Transfer characteristics of (a) TIPS-Tc/IGZO at V_{ds} = 1 V measured in the dark, under 535 nm illumination, and after light-off; (b) TES-ADT/IGZO at V_{ds} = 5 V measured in the dark, under 545 nm illumination, and after light-off, which fully returns to the initial dark curve; and (c) a bare IGZO device at V_{ds} = 1 V measured in the dark and under 535 nm illumination, with all illuminations at 10 μW cm^{-2}. (d) Steady-state photoluminescence (PL) spectra of a bare TIPS-Tc film and a TIPS-Tc/IGZO heterojunction (inset: transient PL decay). Drain-current transients of (e) the TIPS-Tc/IGZO device under a 50 s light pulse (535 nm, 1 μW cm^{-2}) at V_g = 0 V and V_{ds} = 1 V, and (f) the TES-ADT/IGZO device under a 5 s light pulse (532 nm, 100 μW cm^{-2}) at V_g = 0 V and V_{ds} = 5 V. Illumination and biasing conditions were chosen to enable fair comparison and to highlight how different organic photoactive layers give rise to trap-induced memory behavior or photodetection.

were fitted with a bi-exponential function, and amplitude-weighted average lifetimes were extracted.

Time-dependent current responses are shown in Fig. 2e and f. Under a 10 s light pulse, the TIPS-Tc/IGZO device exhibits a near-linear photocurrent rise followed by a slow decay after illumination, indicating the accumulation of long-lived holes in deep traps that enhance persistent photogating. In contrast, the TES-ADT/IGZO device responds rapidly under a 5 s pulse, suggesting fewer deep-trap contributions. To quantitatively interpret these behaviors, we developed a model that extracts trapped-charge density in the organic layer from the transient drain current $I_{ds}(t)$ and solves coupled rate equations for shallow and deep trapping and detrapping, enabling quantitative prediction of device dynamics.

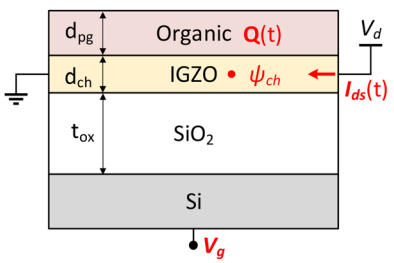

Fig. 3 Schematic illustration of the phototransistor structure used to model the transient drain current $I_{ds}(t)$ modulated by photogenerated charge $Q(t)$ trapped in the organic layer and applied gate bias V_g, which together set the channel potential ψ_{ch}. The model includes an organic layer, IGZO channel, and gate oxide with thicknesses d_{pg}, d_{ch}, and t_{ox}, respectively.

2.2 Analytical framework relating photogenerated charge to device transfer characteristics

In a photogated IGZO TFT, the channel potential ψ_{ch} is modulated by both the bottom gate voltage V_g coupled through the gate oxide capacitance per area C'_{ox} and the total (shallow and deep) trapped photogenerated holes $Q(t)$ in the organic layer of thickness d_{pg} (Fig. 3). Assuming negligible depletion in the IGZO layer and uniform electron concentration n_{ch} across the channel thickness d_{ch}, the total channel electron charge per unit area is

$$Q'_n = -qn_{ch}d_{ch}.$$

This uniform-density approximation is justified for the thin IGZO film used here (d_{ch} = 25 nm), where the vertical potential

drop is small. This is further supported by our previous device simulations,[12] which show that under subthreshold V_g operation, a nearly uniform electron distribution is maintained across the thin IGZO layer, even in the presence of photogating. Under this condition, the channel charge must balance the gate-induced and photogate-induced electrostatic charges:

$$Q'_n(t) = -\left[C'_{ox}\left(V_g - \psi_{ch}(t)\right) + \alpha q Q(t) d_{pg}\right].$$

where α is a V_g-dependent correction factor that reflects how the gate field electrostatically governs the spatial distribution of the trapped charges in the organic layer and thereby influences the photogating efficiency. Specifically, $\alpha = 1$ when $V_g = 0$, $\alpha > 1$ for $V_g < 0$, and $\alpha < 1$ for $V_g > 0$. A negative V_g drives trapped holes in the organic layer toward the interface, enhancing their electrostatic coupling with the channel and, consequently, the photogating efficiency. In contrast, a positive V_g pushes trapped holes away from the interface, weakening their coupling to the channel and reducing the photogating effect.

Substituting yields the charge–potential balance relation

$$q n_{ch}(t) d_{ch} = C'_{ox}\left[V_g - \psi_{ch}(t)\right] + \alpha q Q(t) d_{pg}. \quad (1)$$

The channel potential relates to electron density *via* Boltzmann statistics:

$$\psi_{ch}(t) = \frac{kT}{q}\ln\left(\frac{n_{ch}(t)}{n_0}\right).$$

where n_0 is the equilibrium channel electron density when $\psi_{ch} = 0$. Substituting into eqn (1) yields a self-consistent expression for $n_{ch}(t)$:

$$q n_{ch}(t) d_{ch} + C'_{ox}\frac{kT}{q}\ln\left(\frac{n_{ch}(t)}{n_0}\right) = \alpha q Q(t) d_{pg} + C'_{ox} V_g. \quad (2)$$

Eqn (2) yields

$$n_{ch}(t) = \frac{B}{A} W_0\left(n_0 \frac{A}{B} e^{\frac{C}{B}}\right) \quad (3)$$

where $W_0(\cdot)$ is the Lambert W function and

$$A = q d_{ch}, \quad B = C'_{ox}\frac{kT}{q}, \quad C = \alpha q Q(t) d_{pg} + C'_{ox} V_g.$$

Under subthreshold conditions and small drain bias V_{ds}, the drain current is proportional to the channel electron density:

$$I_{ds}(t) = q n_{ch}(t) d_{ch} \mu \frac{W}{L} V_{ds}, \quad (4)$$

with μ, W, and L being the electron mobility in the IGZO channel, channel width, and length, respectively. Substituting eqn (3) into (4) gives

$$I_{ds}(t) = K_{ch}\frac{B}{A} W_0\left(n_0 \frac{A}{B} e^{\frac{C}{B}}\right), \quad (5)$$

where $K_{ch} = q d_{ch} \mu (W/L) V_{ds}$ is a proportionality factor set by the channel geometry and carrier mobility. The inverse relation provides the trapped-charge density as a function of the transient drain current $I_{ds}(t)$:

$$Q(t) = \frac{1}{\alpha}\left[\frac{C'_{ox}}{q d_{pg}}\left(\ln(10)\frac{kT}{q}\log\left(\frac{I_{ds}(t)}{n_0 K_{ch}}\right) - V_g\right) + \frac{d_{ch}}{d_{pg}}\frac{I_{ds}(t)}{K_{ch}}\right]. \quad (6)$$

The quantity $n_0 K_{ch}$ corresponds to the drain current in the absence of photogating and gate bias, *i.e.*, when the channel is at its equilibrium electron density occurring at $\psi_{ch} = 0$. Eqn (6) describes how the subthreshold drain current I_{ds} is jointly modulated by the gate voltage V_g and the time-dependent photogenerated trapped charge $Q(t)$ in the organic layer, providing a direct analytical link between the measured transient response and the underlying trap dynamics. It is worth noting that the analytical model is developed for the subthreshold operating condition during drain current measurement and does not apply to monitoring the drain current during large gate biases associated with trapped-charge redistribution in the organic layer.

2.3 Dynamics of photogenerated trapped charge

Photogenerated holes in the organic layer can exist as free or trapped holes. The total hole concentration at any time t is expressed as

$$p_0(t) = p(t) + T(t) + M(t).$$

where $p(t)$ denotes free hole concentration, and $T(t)$ and $M(t)$ represent shallow- and deep-trapped-hole populations, respectively.

2.3.1 Formulation of the photogenerated trapped charge population dynamics. The temporal evolution of the free hole population is governed by the continuity equation, which incorporates photogeneration, recombination, trapping, and detrapping processes:

$$\begin{aligned}\frac{dp(t)}{dt} &= g(t) - \frac{p(t)}{\tau_R} - \gamma_T p(t)[T_0 - T(t)] \\ &\quad - \gamma_M p(t)[M_0 - M(t)] + \beta_T T(t) + \beta_M M(t)\end{aligned} \quad (7)$$

where $g(t)$ is the volumetric photogeneration rate, τ_R is the free carrier recombination lifetime, $\gamma_{T,M}$ and $\beta_{T,M}$ are the trapping and detrapping rate coefficients for shallow (T) and deep (M) traps, and T_0 and M_0 are the total available shallow and deep trap densities, respectively. Under moderate illumination, recombination dominates over trapping and detrapping ($1/\tau_R \gg \gamma_T T_0$, $\gamma_M M_0$, β_T, β_M), allowing the free-hole population to decouple from the trap dynamics. The free hole density rapidly reaches a steady-state value of $p(t) \approx g_0 \tau_R$ during illumination, where g_0 is the generation rate determined by the optical power density and absorption properties of the organic layer. After the light is turned off, $p(t)$ rapidly drops to zero compared to the trapping timescale.

Substituting this quasi-steady $p(t)$ into the continuity equations for trapped holes yields first-order rate equations:

$$\frac{dT(t)}{dt} = k_T(T_0 - T(t)) - \beta_T T(t),$$
$$\frac{dM(t)}{dt} = k_M(M_0 - M(t)) - \beta_M M(t) \quad (8)$$

with $k_T = \gamma_T g_0 \tau_R$ and $k_M = \gamma_M g_0 \tau_R$ defining the effective shallow and deep trap-filling rates, respectively (derived in SI, eqn (S3)–(S7)). Solving eqn (8) for illumination ($0 \le t \le t_p$) and post-illumination ($t > t_p$) gives

$$T(t) = \begin{cases} T_{ss} + (T_i - T_{ss})e^{-(k_T+\beta_T)t} & 0 \le t \le t_p \\ T(t_p)e^{-\beta_T(t-t_p)} & t > t_p \end{cases}, \quad (9a)$$

$$M(t) = \begin{cases} M_{ss} + (M_i - M_{ss})e^{-(k_M+\beta_M)t} & 0 \le t \le t_p \\ M(t_p)e^{-\beta_M(t-t_p)} & t > t_p \end{cases}, \quad (9b)$$

where $T_{ss} = k_T T_0/(k_T + \beta_T)$ and $M_{ss} = k_M M_0/(k_M + \beta_M)$ are steady-state trap occupancies under continuous illumination. The total trapped-hole density is the sum of the two components:

$$Q(t) = T(t) + M(t), \quad (9c)$$

which exhibits a biexponential temporal behavior with a fast component from shallow traps and a slow component from deep traps.

2.3.2 Dynamics of photogenerated trapped charge under repetitive illumination. Under periodic optical excitation with a pulse period t_p and light-on duration t_{on}, the trapped-hole populations evolve recursively, and their concentrations after the $(n + 1)$-th illumination cycle are given by:

$$T_{n+1} = T_n \eta_{on,T} \eta_{off,T} + T_{ss}(1 - \eta_{on,T})\eta_{off,T}, \quad (10a)$$

$$M_{n+1} = M_n \eta_{on,M} \eta_{off,M} + M_{ss}(1 - \eta_{on,M})\eta_{off,M} \quad (10b)$$

with $\eta_{on,i} = e^{-(k_i+\beta_i)t_{on}}$ and $\eta_{off,i} = e^{-\beta_i(t_p - t_{on})}$ are the light- and dark-phase retention factors for shallow (i = T) and deep (i = M) traps (SI, eqn (S13)–(S16)). The factor $\eta_{on,i}$ quantifies how much of the previously trapped holes persist through illumination, while $\eta_{off,i}$ characterizes the fraction retained during the dark period due to finite detrapping. Together, these parameters govern the evolution of total trapped hole concentration across successive optical cycles, capturing the balance between short-term decay and long-term memory retention in the hybrid heterojunction phototransistor:

$$Q_{n+1} = T_{n+1} + M_{n+1}. \quad (11)$$

Once Q is determined, it directly couples to the channel electrostatics through eqn (5), enabling quantitative prediction of the transient drain-current response $I_{ds}(t)$ under arbitrary illumination waveforms. Full derivations and intermediate steps are provided in SI, Section S2 (eqn (S1)–(S17)).

2.3.3 Interpretation of the photoinduced memory effect. The recurrence relations in eqn (10) describe how the trap states at the beginning of the $(n + 1)$-th cycle result from a balance between memory retained from the previous pulse and the new charge accumulated during the current illumination. The factors η_{on} and η_{off} serve as retention weights that determine how prior and present inputs shape the trap evolution over time. A larger trapping rate k (faster hole capture) or detrapping rate β (faster release) decreases η_{on}, indicating a stronger update toward the steady-state trap occupancy T_{ss} or M_{ss}, and a weaker dependence on the previous state T_n or M_n. This reduction in η_{on} reflects accelerated convergence to a new equilibrium, not physical erasure of prior trapped holes. A value of $\eta_{on} \approx 1$ implies slow updating and strong memory retention, whereas $\eta_{on} \ll 1$ reflects rapid response to light exposure and limited influence from earlier pulses.

On the other hand, the dark-phase factor η_{off} depends solely on the detrapping rate β and the dark duration t_p–t_{on}, governing how much of the trap state, whether originating from memory or new accumulation, is preserved until the start of the next cycle. A value of $\eta_{off} \approx 1$ suggests excellent retention of trapped holes during the dark period, while $\eta_{off} \ll 1$ corresponds to significant memory loss due to hole detrapping.

Together, these factors define two distinct contributions in the recurrence model: (1) the residual memory from the prior state, T_n or M_n, carried forward with weight $\eta_{on,i}\eta_{off,i}$, where i = T, M; and (2) the newly accumulated holes during the current light pulse, $T_{ss}(1 - \eta_{on,T})$ or $M_{ss}(1 - \eta_{on,M})$, which persists through the dark period scaled by η_{off}, and adds to the trapped hole level at the start of the next cycle.

The interplay between η_{on} and η_{off} dictates whether the device exhibits short- or long-term photoinduced memory. When both factors approach unity, corresponding to small k and β, *i.e.*, deep-trap-dominated behavior ($k_M \ll k_T$ and $\beta_M \ll \beta_T$), the trapped charge evolves slowly and remains well preserved, producing long-term memory. In contrast, when both factors are much less than one, reflecting shallow traps with rapid trapping and detrapping, the system exhibits short-term memory characterized by fast adaptation and rapid decay between optical pulses.

2.4 Biexponential trap-dynamics model fitting

To validate the model described in Section 2.3, experimental data from hybrid organic–inorganic phototransistors were fitted using the analytical framework. Fig. 4a shows the total trapped charge density $Q(t)$, derived from the transient drain current of a TIPS-Tc/IGZO device under a 50 s optical pulse (535 nm, 1 μW cm^{-2}), together with the fitted curve. The agreement is excellent ($R^2 = 0.998$), confirming the high fidelity of the model. The nearly linear photoresponse and slow post-illumination decay further indicate that TIPS-Tc/IGZO exhibits persistent photogating suitable for synaptic device operation.

Fig. 4b presents $Q(t)$ and the corresponding fit ($R^2 = 0.984$) for a TES-ADT/IGZO device under a single 5 ms optical pulse (525 nm, 1 mW cm^{-2}). The faster rise and decay dynamics highlight its suitability for photodetection operation and demonstrate the model's accuracy and versatility across materials. Details of Q, T_0, and M_0 extraction procedures are provided in the Methods section, and the fitted parameters are summarized in Table 1.

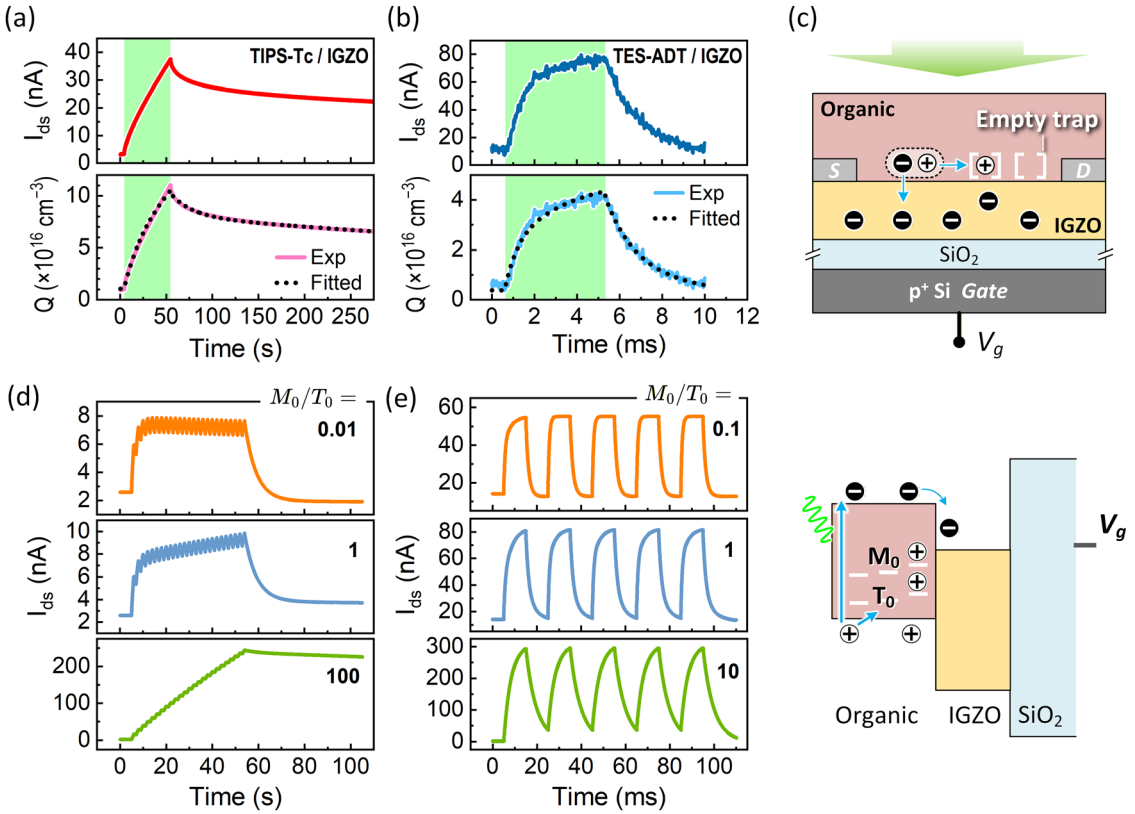

Fig. 4 (a) Transient drain current $I_{ds}(t)$ and extracted trapped-hole density $Q(t)$ for a TIPS-Tc/IGZO device under a single 10 s optical pulse (535 nm, 1 μW cm^{-2}). (b) Transient $I_{ds}(t)$ and $Q(t)$ for a TES-ADT/IGZO device under a single 5 ms optical pulse (525 nm, 1 mW cm^{-2}). (c) Schematic and band diagram illustrating photo-induced charge transfer and trap-assisted photogating in the organic/inorganic heterojunction. (d) Simulated TIPS-Tc/IGZO device response to 25 consecutive optical pulses (2 s period, 1 s width) for deep-to-shallow trap density ratios M_0/T_0 = 0.01, 1, 100 with T_0 = 1.04 × 10^{17} cm^{-3}. (e) Simulated TES-ADT/IGZO device response to 5 consecutive optical pulses (20 ms period, 10 ms width) for M_0/T_0 = 0.1, 1, 10 with T_0 = 4.75 × 10^{16} cm^{-3}. All measurements and simulations were performed at V_g = 0 V, V_{ds} = 1 V.

Table 1 Fitted trap-kinetic parameters revealing shallow- and deep-trap dynamics in TIPS-Tc/IGZO and TES-ADT/IGZO phototransistors at V_g = 0 V

Parameters	k_T (s^{-1})	k_M (s^{-1})	β_T (s^{-1})	β_M (s^{-1})	T_0 (cm^{-3})	M_0 (cm^{-3})
TIPS-Tc	1.35×10^{-2}	3.50×10^{-4}	4.24×10^{-2}	9.07×10^{-4}	1.04×10^{17}	3.03×10^{18}
TES-ADT	1.05×10^{3}	1.05×10^{2}	7.40×10^{2}	2.07×10^{2}	4.75×10^{16}	5.76×10^{16}

The fitted trapping (k) and detrapping (β) constants represent per-trap capture and emission rates, respectively. The trapping constant k is governed by the effective capture cross section, determined by the wavefunction overlap between the trap state and the HOMO-derived states responsible for hole conduction. The detrapping constant β is primarily controlled by the emission barrier, *i.e.*, the trap depth relative to the HOMO level. In general, traps located closer to the HOMO edge exhibit larger emission rates due to smaller activation barriers, while deeper traps exhibit smaller emission rates and longer carrier lifetimes.

As summarized in Table 1, TES-ADT/IGZO exhibits trapping and detrapping rates that are several orders of magnitude larger than those of TIPS-Tc/IGZO, indicating substantially smaller emission barriers and faster carrier release. Within TES-ADT, the shallow and deep detrapping constants differ by less than one order of magnitude ($\beta_T/\beta_M \approx 3.6$) and the corresponding trap densities are comparable ($T_0 \approx M_0$), implying similar trap depths located near the HOMO level. Although the energetic distinction between the two trap populations is limited, the trapping rates remain moderately distinct ($k_T/k_M \approx 10$), reflecting differences in effective capture cross section rather than emission barrier height. Consequently, despite their similar detrapping rates, the two trap populations exhibit different trapping efficiencies. This kinetic distinction necessitates a biexponential model to accurately reproduce the transient response and is consistent with the rapid rise and recovery observed in TES-ADT.

In contrast, TIPS-Tc exhibits a much stronger separation between shallow and deep detrapping rates ($\beta_T/\beta_M \approx 50$) with an extremely low deep-trap detrapping rate. Together with the dominant deep-trap density ($M_0 \gg T_0$), these parameters indicate a broad distribution of trap depths in energy, where deep states possess substantially large emission barriers and

dominate the trapped-charge population. The very small deep-trap emission rate leads to long-lived trapped holes, sustaining persistent photogating and extended retention behavior.

The dominance of deep traps in TIPS-Tc therefore gives rise to slow, persistent photogating behavior that is advantageous for synaptic memory operation, whereas the compressed trap distribution and rapid carrier exchange in TES-ADT result in fast transient response suitable for photodetection. Fig. 4c schematically illustrates the interfacial charge transfer and trap-assisted photogating mechanism, highlighting the relative energetic positions of shallow and deep traps with respect to the HOMO level.

To further assess the effect of deep-trap density, transient responses were simulated under consecutive optical pulses (2 s period, 1 s width) with varying M_0 while keeping all other parameters fixed at their fitted values. Fig. 4d and e show the resulting transient drain currents for three values of the deep-to-shallow trap density ratio M_0/T_0 in TIPS-Tc and TES-ADT devices, respectively. In the TIPS-Tc device (Fig. 4d), a low M_0/T_0 ratio leads to rapid saturation, limited dynamic range, and negligible memory effect, undesirable for synaptic operation. Increasing M_0 produces stronger and more linear incremental responses because a higher deep-trap density provides a larger charge storage capacity and stabilizes the trapped-hole population during each pulse, allowing successive conductance updates to accumulate gradually rather than saturate, a behavior characteristic of synaptic plasticity. In contrast, for TES-ADT (Fig. 4e), deep-trap density primarily governs the rise and fall times of the pulsed response. Reducing M_0 sharpens the transients and increases response speed but lowers signal amplitude and thus sensitivity. These trends demonstrate that lower deep-trap density is beneficial for high-speed photodetection, whereas higher M_0/T_0 enhances sensitivity and enables memory-like behavior.

2.5 Gate-tunable memory and retention modes in TIPS-Tc/IGZO phototransistor

Fig. 5 demonstrates how different gate-voltage modulation schemes control persistent photogating and enable three distinct operating modes in the TIPS-Tc/IGZO phototransistor. Under excitation by a train of optical pulses, the channel conductance progressively increases. After optical stimulation,

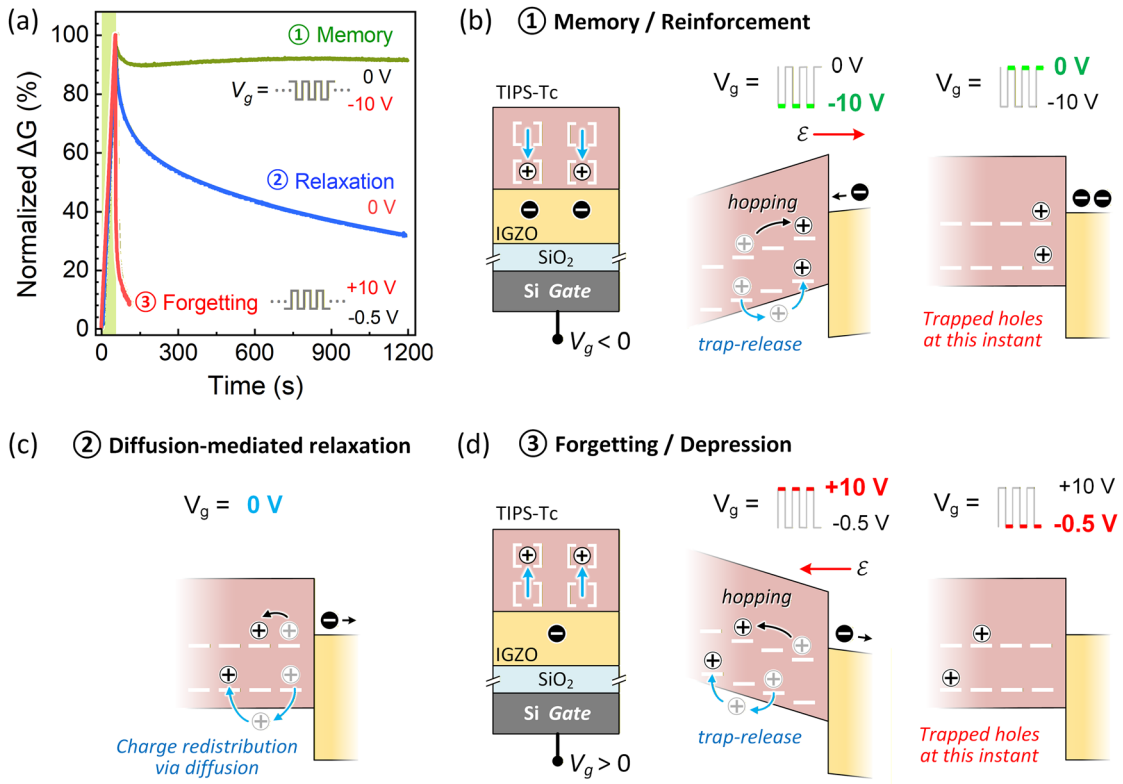

Fig. 5 Operating modes of the TIPS-Tc/IGZO synaptic phototransistor. (a) Normalized channel conductance evolution under pulsed illumination (5 μW cm^{-2}, 1 s pulse width, 2 s period), followed by different post-illumination gate modulations demonstrating three operational modes: memory (cycling V_g between 0 V and −10 V), relaxation (constant V_g = 0 V), and forgetting (cycling V_g between −0.5 V and +10 V). All V_g pulses use a 1 s width and 2 s period; conductance is sampled during low-bias intervals (0 V or −0.5 V) to minimize disturbance. (b) Memory mode: negative V_g attracts trapped holes toward the TIPS-Tc/IGZO interface, reinforcing photogating and maintaining high channel conductance through continuous replenishment from the bulk. (c) Relaxation mode: with V_g = 0 V, trapped holes gradually detrap and recombine—fast release from shallow states followed by slower decay from deep traps—leading to natural conductance decay. (d) Forgetting mode: Positive V_g drives trapped holes away from the interface, weakening capacitive coupling and accelerating detrapping, resulting in rapid conductance decrease. Trapped-hole dynamics follow a biexponential behavior, with shallow traps relaxing *via* fast multiple-trapping-and-release and deep traps *via* slower hopping-mediated pathways.

the device operates one of three post-illumination gate-bias schemes: negative pulsed V_g sequence (from 0 V to −10 V), static zero bias (V_g = 0 V), or positive pulsed V_g sequence (from −0.5 V to +10 V) to implement memory, relaxation, and forgetting modes, respectively. During pulsed-gate operations, conductance is sampled at the low-bias level (0 V or −0.5 V), which is substantially smaller in magnitude than the programming pulses (±10 V) to avoid disturbing the trapped charge distribution in the organic layer. Fig. 5a compares the normalized conductance evolution, with temporal scaling referenced to the onset of gate modulation, highlighting the distinct response behaviors. Raw conductance traces are provided in SI Fig. S2.

In memory mode, V_g alternates between 0 V and −10 V (1 s each), with conductance sampled at 0 V. Under this pulsed-bias condition, the device retains ∼94% of its post-illumination conductance even after more than 1000 s. In relaxation mode, a static V_g = 0 V causes the conductance to gradually decay to below 40% over the same period. In forgetting mode, V_g oscillates between −0.5 V and 10 V (1 s each), leading to rapid conductance suppression, with >50% reduction after a single pulse and down to ∼7% after 50 pulses. Sampling at −0.5 V accentuates the suppressed state, whereas sampling at 0 V gives a similar trend but with slightly higher conductance due to bias being closer to the channel activation threshold. These results confirm that tailored V_g modulation provides effective control over persistent photogating, enabling the device to switch between memory-like retention and rapid conductance decay, supporting synaptic function with faster and more precise conductance control.

Fig. 5b illustrates the mechanism underlying the reinforced memory mode. Under a large negative gate bias (−10 V), the electric field drives photogenerated trapped holes from the TIPS-Tc bulk toward the interface. Hole transport proceeds *via* two field-assisted pathways: rapid migration through shallow trap states through multiple-trapping-and-release (MTR), and slower hopping between deep localized states. This continuous supply of holes to interfacial traps replenishes detrapped charge, maintaining strong photogating. Analogous to DRAM refresh, the TIPS-Tc layer serves as a hole reservoir, while periodic negative V_g pulses act as a refresh stimuli that stabilize channel conductance. As a result, the device exhibits highly stable, long-term retention under pulsed-gate operation. By modulating the gate waveform, the phototransistor can be reconfigured between transient (short-term) and persistent (long-term) memory modes, enabling programmable light-driven synaptic functionality.

Fig. 5c shows the relaxation phase under V_g = 0 V. After light-off, photogenerated holes trapped in the TIPS-Tc layer gradually detrap or recombine. Holes in shallow trap states release quickly, causing an initial rapid conductance decrease, whereas those in deeper traps dissipate more slowly, giving rise to a prolonged exponential-like decay. As trapped holes vanish, the photogating effect weakens, and the IGZO channel conductance follows a bi-exponential decay, consistent with the coexistence of shallow and deep trap populations and their distinct release dynamics.

During the forgetting mode (Fig. 5d), a positive gate bias (+10 V) drives photogenerated holes away from the TIPS-Tc/IGZO interface. This actively suppresses photogating: shallow traps empty quickly *via* rapid MTR transport, resulting in an abrupt conductance decrease during initial pulse cycles, while deeper traps respond more slowly, forming a gradual decay tail. Positive V_g pulsing, therefore, accelerates charge redistribution and memory erasure, enabling fast conductance recovery.

To verify that the conductance suppression responsible for the forgetting process under high positive gate bias is reversible rather than due to irreversible IGZO degradation, repeated optical potentiation–electrical depression (LTP–LTD) cycles were performed. As shown in SI Fig. S3, three consecutive cycles exhibit nearly identical peak conductance and closely overlapping conductance evolution across the potentiation, peak, and depression stages, with no cumulative amplitude loss or progressive degradation. This confirms that high positive gate bias does not induce irreversible bias-stress effects in the IGZO channel. Instead, the conductance suppression originates from reversible weakening of persistent photogating *via* gate-driven redistribution and detrapping of photogenerated holes in the organic layer.

3. Conclusion

The proposed current-to-charge conversion method, combined with a biexponential trap-dynamics model, provides a clear and quantitative framework for understanding the operation of hybrid organic–inorganic phototransistors. By directly linking material properties to measured device response using only a few kinetic parameters, the model enables rapid interpretation with strong physical relevance. In TIPS-Tc/IGZO devices, persistent photogating arising from deep traps explains the refreshable memory behavior and near-linear synaptic conductance modulation, whereas in TES-ADT/IGZO devices, the same framework accurately captures the fast, detector-like response dominated by shallow traps. The design rules are straightforward: increasing the density of deep traps enhances retention and linearity, enabling memory-like behavior, while reducing deep-trap density improves response speed at the expense of sensitivity, favoring photodetection. Accordingly, the deep-to-shallow trap density ratio serves as a key parameter defining the trade-off between synaptic memory performance and detection sensitivity. Because the approach relies on minimal transient measurements and yields kinetic parameters with clear physical meaning, it can be readily extended to other organic–oxide systems, scaled for array-level modeling, and applied to materials screening and process optimization. Overall, this framework serves not only as a quantitative explanatory model but also as a practical design guide for engineering light-programmable optoelectronic memory and high-speed photodetector devices.

4. Method

4.1 Device fabrication

Heterojunction phototransistors were fabricated following our previously reported protocol[12] with the key steps summarized

here. Bottom-gate IGZO TFTs were prepared on heavily doped p-type Si substrates with a 300 nm SiO_2 gate dielectric. The substrates were sequentially cleaned by solvent sonication, dried under N_2, and prebaked to remove residual moisture. A 25 nm IGZO channel layer was deposited by RF magnetron sputtering from an In : Ga : Zn (1 : 1 : 1) target in an Ar/O_2 ambient through a shadow mask, followed by thermal annealing at 400 °C to activate the film. The sputtering oxygen partial pressure during sputtering and post-deposition annealing conditions was optimized to suppress dark current and enhance photodetectivity. Aluminum source/drain contact electrodes were thermally evaporated to define channels with a length of 100 μm and a width of 1000 μm.

Before heterojunction formation, a brief dehydration bake was performed to minimize adsorbed moisture, which can cause charge trapping and threshold voltage shifts in oxide TFTs. A 50 nm thick photosensitive organic layer of TIPS-Tc or TES-ADT blended with poly(methyl methacrylate) (PMMA) was spin-cast onto the IGZO layer at 1500 rpm. The blend concentration corresponds to an average intermolecular spacing of ~1 nm in the film.[24] The film was then soft-baked in the dark at 85 °C for 10 min to remove residual solvent. All fabrication steps were conducted in a nitrogen glovebox. Residual organic material on the contact pads was removed using an acetone-dampened swab. Optical and electrical measurements were performed under ambient conditions.

4.2 Optoelectronic and electrical characterization

Optical absorption spectra were acquired using a tungsten–halogen lamp as a light source, with the incident beam focused to a near-diffraction-limited spot (<5 μm) through a 10× objective lens. Reflected light was dispersed and detected using a SpectraPro HRS-300 spectrograph. Photoluminescence (PL) was excited using 450 nm pulses (100–180 fs, 10 kHz repetition rate) generated by a second-harmonic generation (APE HarmoniXX) from a femtosecond optical parametric amplifier (OPA, ORPHEUS-F, Light Conversion). The excitation beam was focused onto the sample, and PL emission was collected along the same optical path as in the absorption measurements. A 500 nm long-pass filter was inserted in the collection path to block the excitation pump.

Time-resolved photoluminescence (PL) was measured using a time-correlated single-photon counting (TCSPC) system. Samples were excited with a 532 nm picosecond pulsed beam from a frequency-doubled Nd:YAG laser (500 kHz, HE-1060). The emitted photons passed through a 532 nm long-pass filter before being detected using a single-photon avalanche photodiode (SPAD; Molecular Photonic Devices) with arrival times recorded by a TCSPC module (TimeHarp 200, PicoQuant Inc.). The instrument response function (IRF) provided an effective temporal resolution of approximately 380 ps.

Current–voltage (*I–V*) measurements were conducted using a Keithley 2636B sourcemeter with a custom probe adapter. For wavelength-resolved excitation, light from a Horiba FluoroMax-4 fluorospectrometer equipped with an integrated monochromator and an ozone-free xenon arc lamp was focused onto the device using a 4× objective lens. A neutral-density filter was used to maintain a constant incident power density across all wavelengths. Time-resolved photocurrent transients were recorded using a Keithley 2400 sourcemeter.

4.2.1 Trapped hole density (Q) extraction from drain current (I_{ds}). The time-dependent trapped-hole density $Q(t)$ was extracted from the measured drain current $I_{ds}(t)$ using eqn (6). In the equation, K_{ch} is a current proportionality factor that captures the geometric and mobility-dependent channel conductance, while n_0 represents the equilibrium electron density in the absence of photogenerated trapped charge, under the built-in heterojunction potential when the organic layer is fully detrapped ($Q \approx 0$). These two parameters were calibrated using a bare IGZO reference device. By differentiating eqn (6) with respect to I_{ds} at the detrapped condition ($Q(t) = 0$), we obtain:

$$K_{ch} = m\left(\frac{dV_g}{dI_{ds}} - \frac{V_T}{I_{ds}}\right)^{-1}, \quad n_0 = \frac{I_{ds}}{K_{ch}} e^{\left(m\frac{I_{ds}}{K_{ch}} - V_g\right)\Big/ V_T}$$

where $m = qd_{ch}/C'_{ox}$, $V_T = kT/q$ and both dV_g/dI_{ds} and I_{ds} were evaluated at $V_g = 0$ V using the transfer characteristics of the detrapped bare IGZO reference device.

4.2.2 Extraction of parameter α. The parameter α accounts for the gate-bias–dependent redistribution of trapped holes in the organic layer and its influence on channel conductance. By definition, $\alpha = 1$ at $V_g = 0$, and its value at other gate biases is obtained by scaling relative to this reference. Eqn (6) is first evaluated at $V_g = 0$ with $\alpha = 1$, establishing the baseline conversion between $I_{ds}(t)$ and $Q(t)$ in the zero bias state. For other gate voltages ($V_g = -0.5$, 0.5 V), an effective trapped charge density $Q_{eff}(V_g, t)$ is computed using this same reference relation. The gate-dependent scaling factor is then determined from the initial values:

$$\alpha(V_g) = \frac{Q_{eff}(V_g, t = 0)}{Q_{eff}(V_g = 0, t = 0)}.$$

The actual trapped-hole density is finally obtained by applying this scaling:

$$Q(V_g, t) = \frac{Q_{eff}(V_g, t)}{\alpha(V_g)}.$$

4.2.3 Extraction of shallow and deep trap densities T_0 and M_0. The total trap populations were extracted by solving a coupled set of equations derived from fitting the transient response to eqn (9) over both the illumination period ($0 \le t \le t$) and the decay period ($t > t$):

$$a_T T_i + T_{ss}(1 - a_T) = T(t_p), \quad a_M M_i + M_{ss}(1 - a_M) = M(t_p) \tag{12a}$$

$$T_i - T_{ss} = Q_s, \quad M_i - M_{ss} = Q_d \tag{12b}$$

where $a_T = e^{-(k_T+\beta_T)t_p}$ and $a_M = e^{-(k_M+\beta_M)t_p}$. The quantities $T(t_p)$, $M(t_p)$, β_T and β_M were obtained by fitting the post-illumination decay region ($t > t_p$), whereas Q_s, Q_d, k_T and k_M were extracted from fitting the eqn (6) during illumination $0 \le t \le t_p$.

Solving eqn (12a) and (12b) yields the initial (i) and steady-state (ss) trapped-hole populations:

$$T_i = T(t_p) + Q_s\left(1 - e^{-(k_T+\beta_T)t_p}\right), \quad T_{ss} = T(t_p) - Q_s e^{-(k_T+\beta_T)t_p}$$

$$M_i = M(t_p) + Q_d\left(1 - e^{-(k_M+\beta_M)t_p}\right),$$
$$M_{ss} = M(t_p) - Q_d e^{-(k_M+\beta_M)t_p}.$$

Finally, using the steady-state solution to eqn (8), the shallow- and deep-trap state densities were determined as:

$$T_0 = \left(1 + \frac{\beta_T}{k_T}\right) T_{ss}, \quad M_0 = \left(1 + \frac{\beta_M}{k_M}\right) M_{ss}.$$

Conflicts of interest

There are no conflicts to declare.

Data availability

The data supporting the findings of this study are available within the article and its supplementary information (SI). Supplementary information: includes steady-state photoluminescence spectra of pristine TES-ADT and TES-ADT/IGZO heterojunction films (Fig. S1), raw channel-conductance traces of the TIPS-Tc/IGZO phototransistor operated in memory mode (Fig. S2a), sampled channel conductance evolution under different gate voltages (Fig. S2b and c), reversibility and repeatability of photoconductance modulation under repeated potentiation–depression cycles (Fig. S3), and the full derivation of the biexponential trap-dynamics model. See DOI: https://doi.org/10.1039/d5tc04439a.

Acknowledgements

The authors thank Prof. J. Anthony for the TIPS-Tc derivatives and Rick Presley and Chris Tasker for their assistance with the RF sputtering and thermal evaporation tools. This work was supported in part by the National Science Foundation (NSF) (CHE-1956431 to O. O). Part of this research was conducted at the Northwest Nanotechnology Infrastructure, a National Nanotechnology Coordinated Infrastructure (NNCI) site at Oregon State University, supported in part by NSF grant NNCI-2025489 and Oregon State University.

References

1 N. Yang, Y. Cui, W. Fu, X. Ma, T. Zhang, W. Wang, Y. Xiao, Z. Chen, Q. Kang, G. Zuo and J. Hou, *ACS Energy Lett.*, 2025, **10**, 2468.
2 Y. Xu, Y. He, D. Shan, B. Zeng and Q.-X. Ni, *ACS Appl. Mater. Interfaces*, 2025, **17**, 4290.
3 H. Zheng, Y. Xiong, Z. Jiang, M. Yu, Q. Hu, Y. Liu and H. Wang, *ACS Appl. Electron. Mater.*, 2025, **7**, 6207.
4 Y. Tang, Y. Song and K. Nomura, *ACS Appl. Mater. Interfaces*, 2025, **17**, 47170.
5 D. Geng, K. Wang, L. Li, K. Myny, A. Nathan, J. Jang, Y. Kuo and M. Liu, *Nat. Electron.*, 2023, **6**, 963.
6 V. Coropceanu, J. Cornil, D. A. Da Silva Filho, Y. Olivier, R. Silbey and J.-L. Brédas, *Chem. Rev.*, 2007, **107**, 926.
7 J. Rivnay, S. C. B. Mannsfeld, C. E. Miller, A. Salleo and M. F. Toney, *Chem. Rev.*, 2012, **112**, 5488.
8 Y. Huang, K. Wu, Y. Sun, Y. Hu, Z. Wang, L. Yuan, S. Wang, D. Ji, X. Zhang, H. Dong, Z. Gong, Z. Li, X. Weng, R. Huang, Y. Cui, X. Chen, L. Li and W. Hu, *Nat. Commun.*, 2024, **15**, 626.
9 C. Chen, Z. Yang, T. Hang, Y. Hao, Y. Chen, C. Zhang, J. Yang, X. Liu, X. Li and G. Cao, *Light: Sci. Appl.*, 2025, **14**, 265.
10 D. Li, Z. Jia, Y. Tang, C. Song, K. Liang, H. Ren, F. Li, Y. Chen, Y. Wang, X. Lu, L. Meng and B. Zhu, *Nano Lett.*, 2022, **22**, 5434.
11 L. Wang, F. Chen, B. Zhou, H. Xu, J. Meng and F. Li, *ACS Appl. Mater. Interfaces*, 2025, **17**, 45968.
12 A. Ullah, R. Lamug, X. Zhang, O. Ostroverkhova and L.-J. Cheng, *Adv. Opt. Mater.*, 2025, **13**, 2500081.
13 C. P. Theurer, A. M. Valencia, J. Hausch, C. Zeiser, V. Sivanesan, C. Cocchi, P. Tegeder and K. Broch, *J. Phys. Chem. C*, 2021, **125**, 6313.
14 Y.-H. Lin, W. Huang, P. Pattanasattayavong, J. Lim, R. Li, N. Sakai, J. Panidi, M. J. Hong, C. Ma, N. Wei, N. Wehbe, Z. Fei, M. Heeney, J. G. Labram, T. D. Anthopoulos and H. J. Snaith, *Nat. Commun.*, 2019, **10**, 4475.
15 H. Li, Z. Wang, Y. Zhao, D. Geng, D. Ji and W. Hu, *Adv. Devices Instrumentation*, 2025, **5**, 0069.
16 S. Lan, J. Si, Z. Zheng, J. Lin, R. Yu, W. Xu, C. Zhou, X. Cai and W. Liao, *J. Phys. D: Appl. Phys.*, 2025, **58**, 135110.
17 H. F. Haneef, A. M. Zeidell and O. D. Jurchescu, *J. Mater. Chem. C*, 2020, **8**, 759.
18 I. Glowacki, J. Jung, G. Wiosna–Salyga, M. Chapran, M. Chapran, B. G. R. Dupont, B. Luszczynska and J. Ulanski, *Display Imaging*, 2017, **2**, 279.
19 S. Kim, H. Yoo and J. Choi, *Sensors*, 2023, **23**, 2265.
20 C. Li, L. Duan, H. Li and Y. Qiu, *J. Phys. Chem. C*, 2014, **118**, 10651.
21 J. Shin and H. Yoo, *Nanomaterials*, 2023, **13**, 882.
22 Y.-C. Lin, W.-C. Yang, Y.-C. Chiang and W.-C. Chen, *Small Science*, 2022, **2**, 2100109.
23 T. Hamid, M. Kielar, S. D. Yambem and A. K. Pandey, *Adv. Electron. Mater.*, 2021, **7**, 2000824.
24 H. F. Haneef, A. M. Zeidell and O. D. Jurchescu, *J. Mater. Chem. C*, 2020, **8**, 759.